

Impact Excavation on Asteroid 4 Vesta: Hubble Space Telescope Results

Peter C. Thomas,* Richard P. Binzel, Michael J. Gaffey, Alex D. Storrs, Eddie N. Wells, Benjamin H. Zellner

Hubble Space Telescope images of asteroid 4 Vesta obtained during the favorable 1996 apparition show an impact crater 460 kilometers in diameter near the south pole. Color measurements within the 13-kilometer-deep crater are consistent with excavation deep into a high-calcium pyroxene-rich crust or olivine upper mantle. About 1 percent of Vesta was excavated by the crater formation event, a volume sufficient to account for the family of small Vesta-like asteroids that extends to dynamical source regions for meteorites. This crater may be the site of origin for the howardite, eucrite, and diogenite classes of basaltic achondrite meteorites.

Unlike other large asteroids, 4 Vesta (1) has a basaltic surface that retains a record of ancient volcanic activity. During early 1996, Vesta made its closest approach to Earth in nearly a decade, and its topographic features and surface color variations were mapped with the Hubble Space Telescope (HST) Wide-Field Planetary Camera 2 (WFPC2) (2). The goal was to search for signatures of impact and igneous events on Vesta in relation to the formation of other small asteroids having basaltic properties (3).

For our analysis, we used 78 WFPC2 images obtained in May 1996, having a scale of 36 km/pixel in combination with lower resolution images (51 km/pixel) obtained in December 1994 (4). The 1996 images were taken through five filters during six HST orbits (5) and provide coverage of the southern hemisphere (Fig. 1). Typically, images are spaced 6° apart in longitude, and there are four gaps in coverage of about 30°. The combined 1994 and 1996 data provide 134 limb profiles at sub-Earth latitudes of 26°N and 9°S, respectively. Vesta's shape can be fit with an ellipsoid of semi-axes of 289, 280, and 229 km. Uncertainties are ±5 km on the basis of scatter of solutions at similar longitudes and the calibration limit of 0.05 pixel (6). The mass of Vesta is $2.75 \pm 0.24 \times 10^{23}$ g (7) to $2.99 \pm$

0.60×10^{23} g (8). The mean density is thus 3500 ± 400 kg m⁻³ to 3900 ± 800 kg m⁻³, consistent with reported values (1).

Views from 1996 that have been deconvolved with a maximum entropy routine (9) reveal that Vesta has a large depression at far southern latitudes that contains a central elevation and bounding rim (Fig. 1). Other depressions can be seen on the limb. The northern hemisphere limb is smoother; this is a real topographic difference between hemispheres, not a function of the terminator position. The hemispheric difference is also seen in the 1994 data, although at lower resolution.

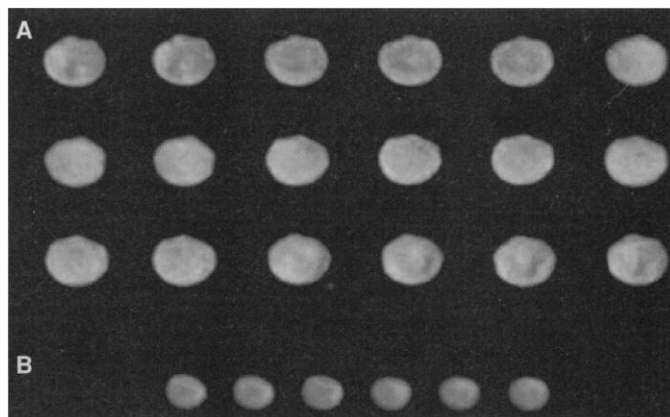
We analyzed Vesta's topography by generating a digital shape model from the original images that reproduces the irregularities of the limb and terminator. We derived a model of Vesta's radius as measured over a 5° × 5° spacing of longitude and latitude, using limb- and terminator-matching techniques (10, 11). For the southern polar re-

gion, the low solar phase angle (5°) of the 1996 observations causes the terminator and actual topographic profiles to be nearly coincident (within 1 km). The most useful measure of long wavelength topography is by reference to some physically meaningful surface, usually an equipotential surface or an ellipsoidal approximation of one. We use dynamic topography (11, 12), which is similar to a measure of heights above an equipotential surface. The computations account for the nonellipsoidal mass distribution, assuming Vesta to be internally homogeneous.

The largest depression resides near the south pole and averages 460 km in diameter; average depth below the rim is 13 km and rim heights above the average surface outside the crater range from 4 to 12 km and average about 7 km (Fig. 2). All relative measures are good to ~3 km. The central peak is about 13 km above the deepest part of the floor. The rim has one region at 320° to 350°W that is ~5 km higher than other parts of the rim. More subtle are variations in floor depth that are possible artifacts due to the effects of longitudinal gaps in coverage and errors in fitting the shape model. Several other depressions, which we interpret as craters, are readily apparent. The largest of these is ~160 km in diameter, 6 km deep, located at 20°N, 70°W and another is ~150 km across, 8 km deep, located at 10°N, 270°W (13).

We interpret the south pole depression as a single crater (14) with a central peak and raised rim. The applicable diameter ranges for transitions of impact features from bowl-shaped simple craters, to central-peaked complex craters, to impact basins with multiple rings primarily scale by the surface gravitational acceleration (15, 16).

Fig. 1. Hubble Space Telescope WFPC2 images of asteroid 4 Vesta obtained in 1996 and 1994. All images presented were taken through the filter F673N and have been processed by a maximum entropy deconvolution. Vesta's south pole is at the top. The images are arranged in longitude order, from left to right and top to bottom, revealing the rotation of albedo features (4, 22). Illumination is from the bottom at



a solar phase angle of 5° in 1996 and from the upper right at 12° in 1994. Central longitudes for 1996 images (A) are, first row: 12°, 26°, 72°, 86°, 99°, and 147°; second row: 160°, 173°, 220°, 233°, 247°, and 250°; and third row: 263°, 277°, 323°, 336°, 350°, and 358°. For 1994 (B), the central longitudes are 221°, 231°, 241°, 284°, 294°, and 305°. The sub-spacecraft latitude in 1994 and 1996 was 26°N and 9°S, respectively. Longitude definitions are from (1).

P. C. Thomas, Center for Radiophysics and Space Research, Cornell University, Ithaca, NY 14853, USA.

R. P. Binzel, Department of Earth, Atmospheric, and Planetary Sciences, Massachusetts Institute of Technology, Cambridge, MA 02139, USA.

M. J. Gaffey, Department of Earth and Environmental Sciences, Rensselaer Polytechnic Institute, Troy, NY 12181, USA.

A. D. Storrs, Space Telescope Science Institute, 3700 San Martin Drive, Baltimore, MD 21218, USA.

E. N. Wells, Astronomy Programs, Computer Sciences Corporation, Space Telescope Science Institute, 3700 San Martin Drive, Baltimore, MD 21218, USA.

B. H. Zellner, Department of Physics, Georgia Southern University, Statesboro, GA 30460, USA.

*To whom correspondence should be addressed.

Central peaks occur in craters of 20 to 140 km in diameter on the moon, up to 80 km in diameter on Mercury, up to 40 km in diameter on Mars, and up to 20 km in diameter on Earth (17, 18). Gravity scaling from the moon (surface gravity, $g = 1.62 \text{ m s}^{-2}$) to Vesta (a mean $g \sim 0.22 \text{ m s}^{-2}$ for a mean density, $\rho = 3500 \text{ kg m}^{-3}$) yields a factor of 7.4 ± 0.8 , where the uncertainty arises from the range of density estimates. Thus the 460-km feature on Vesta would be analogous to a 60-km lunar crater, in the middle of the size range of lunar craters having central peaks. The applicability of gravity scaling of crater morphology from those on the moon to smaller objects has been suggested previously by the bowl-shaped appearance of a 90-km crater on Amalthea (19, 20).

Comparative planetology can also be applied to specific dimensions of Vesta's south pole impact feature. Scaling from fresh 60-km lunar craters would suggest a central peak height of 15 km, consistent with our estimate of 13 km. The relative width of the Vesta crater central peak to the rim diameter (D) is about $0.3 \pm 0.1D$, about the same as the terrestrial planet average (independent of gravity) of 0.22 (18). The average depth of a fresh 60-km lunar crater is 3.6 km (16); scaled to Vesta, this depth corresponds to 27 km, substantially deeper than our estimate of 13 km. However, fresh lunar craters 55 to 65 km in diameter have depths ranging from ~ 2 to 4 km (21) that scale to 15 to 30 km on Vesta. Similarly scaled rim heights on the moon of 1.2 km (16) correspond to 9 km on Vesta, compatible with our estimate of 7 km. Thus, all comparable aspects of the morphology of the Vesta feature are consistent with gravity scaling relative to a 60-km lunar crater.

We used the 0.673-, 0.953-, and 1.042- μm filter images of Vesta to investigate variation in composition with depth for the impact-excavated regions. We applied the same photometric correction, map construction, and normalization techniques used previously (22). By making a ratio of the 0.953- and 1.042- μm images to the 0.673- μm image, we obtained a measure of the depth and width, respectively, of the principal mafic absorption band present in Vesta's spectrum near 1 μm . For each excavated region, we integrated the color ratios along topographic contours to measure compositional variation with depth (Fig. 3) (23). Only the south pole feature shows any significant color variation, where this variation also appears correlated with depth. Within the south pole crater, the absorption band depth and width increases with greater excavation depth, consistent with the exposure of a higher calcium content and coarser grained pyroxene-rich plutonic

assemblage deep within the crust of Vesta or the exposure of olivine present within the upper mantle, or both. The limited number of $<1\text{-}\mu\text{m}$ wavelengths covered by our measurements do not allow us to further distinguish the mineralogy.

The south pole feature has an average depth of about 6 km over its $\sim 1.5 \times 10^5 \text{ km}^2$ area, or a volume of about 10^6 km^3 . This volume can only be related approximately to the ejecta volume because the excavated volume is different from the final crater volume, and because the crater may have been degraded. Some of the highest regions on Vesta are in the crater rim; even with a substantial structural component, several kilometers of ejecta have been deposited near the crater. From the rim height and from scaling to lunar craters (15, 24, 25), we estimate that the ejecta volume was $1.2 \times 10^6 \text{ km}^3$, or $\sim 1\%$ the volume of Vesta. After this redistribution of material, Vesta may not have fully relaxed to an

equilibrium shape: it has an equatorial-to-polar radius ratio that is slightly too large for an equilibrium Maclaurin spheroid, for Vesta's 5.342-hour rotation period and a mean density of 3100 kg m^{-3} or greater (26). Could Vesta maintain a nonequilibrium shape? On the moon, some long-wavelength lunar topography (27) as well as most lunar topography under 500 km in spatial scale is supported by lithospheric strength (28). Such characteristics as lunar flattening, the large relief of major basins, and the support of mascon loads, suggest that viscous relaxation on the moon was effective only for a short time period (29). Additionally, viscous relaxation of large venusian craters is less than other degradational processes such as volcanism (30). The relaxation of Venus topography would be controlled by the strength of dry diabase (31) that may be an appropriate analog for Vesta's composition. Thus, the relief on Vesta is consistent with other planetary

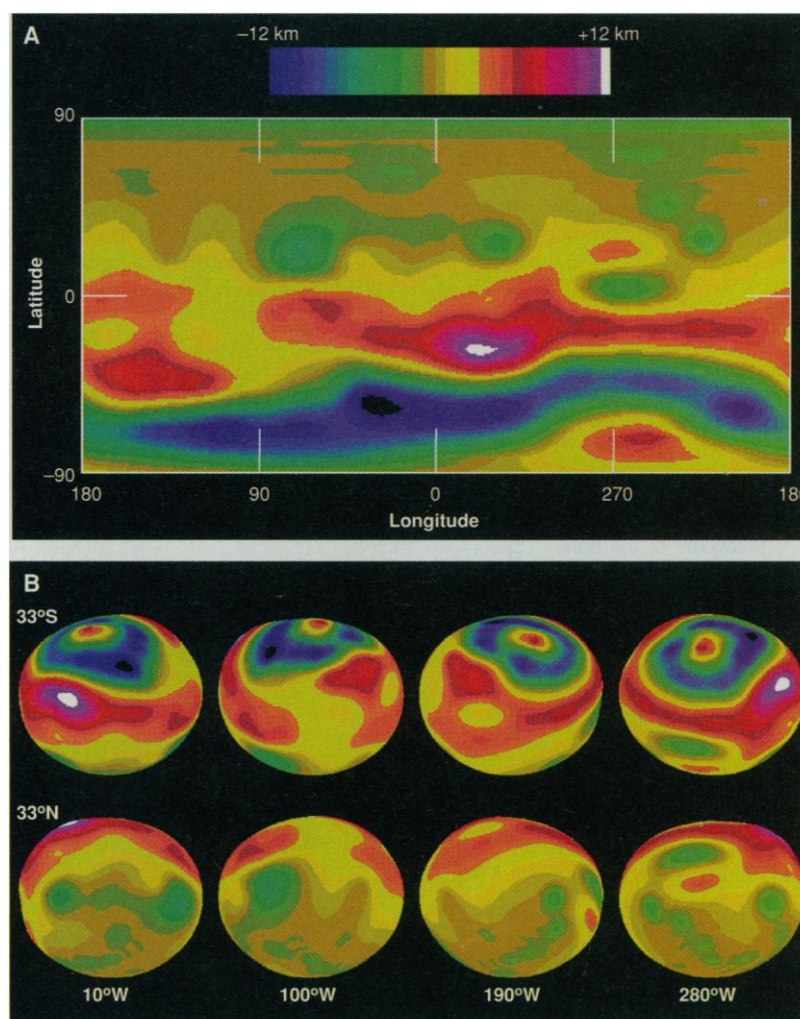


Fig. 2. (A) False-color cylindrical projection of dynamic heights on asteroid 4 Vesta is shown, as measured above and below the mean surface level. (B) Dynamic height solution is projected onto Vesta's shape model and viewed from aspect angles looking from 33°S and 33°N at four different longitudes separated by 90°. South is to the top.

topography. The impact redistribution of mass could have caused some reorientation of principal moments, thus placing the excavated site near the pole, but reorientation of the rotation axis about the maximum moment of inertia is likely to occur in a short time scale for a rigid 500-km body (32).

Interpretation of the south pole feature as an impact crater requires an evaluation of whether Vesta could have survived intact the requisite impact. For complex craters, the transient crater diameter has usually been estimated to be 0.5 to 0.65 of the final crater diameter, on the basis of a variety of observational volume constraints and modeling (33). Thus, we estimate the 460-km Vesta crater had a transient crater of 230 to 300 km diameter; the ratio of the diameter of the transient crater (D_t) to the mean target radius (R) is 0.9 to 1.1, a value not beyond estimates for impact features on other intact solar system bodies (34).

Recent predictions derived by use of smoothed particle hydrocode simulations suggest that large craters relative to the target body size can be formed before the target becomes completely disaggregated (24, 35, 36). Asphaug (37) has modeled an impact on Vesta that forms a transient crater of 270 km diameter as a result of collision with an impactor 34 km in diameter at 5 km s^{-1} . The modeling predicts that Vesta would survive without major disruption or large-scale overturning of the crust. Inde-

pendent hydrocode modeling (38) of near catastrophic collisions of asteroids supports this conclusion. Thus, although Vesta's 460-km-diameter crater is relatively large, it is not uniquely so, and is within theoretical predictions of subcatastrophic (that is, survivable) collisions that may leave most of Vesta's basaltic crust intact.

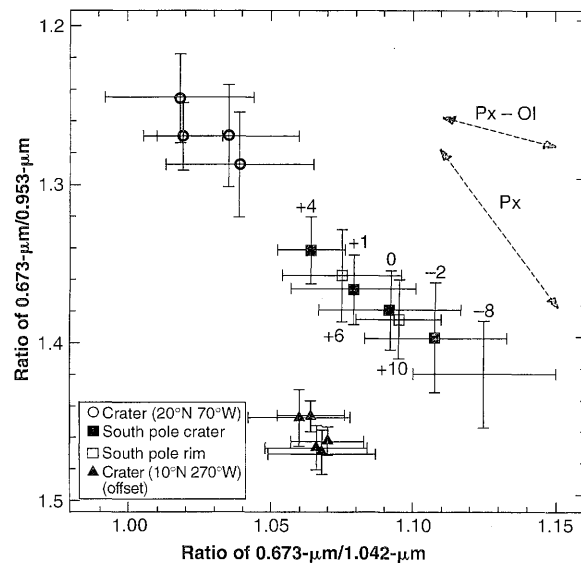
The discovery of substantial impact excavation on Vesta is consistent with our understanding for the origin of basaltic achondrite HED (howardite, eucrite, diogenite) meteorites. Vesta has been suspected as the parent body for these meteorites, which comprise ~6% of all meteorites falling to Earth, based on the similarity of their spectral properties over visible and near-infrared wavelengths (39). Whether material from Vesta could actually reach Earth (40) received observational support with the discovery (3) of more than 20 small (5 to 10 km in diameter) Vesta-like asteroids extending from Vesta to the 3:1 resonance in the main asteroid belt, which is a dynamical escape hatch for providing material to the inner solar system (41). Binzel and Xu (3) proposed that one or more major impact events on Vesta were responsible for creating these observed Vesta-like asteroids, a conclusion supported by subsequent modeling (42). The total volume of these Vesta-like asteroids is only a few percent of the estimated 10^6 km^3 excavated from the south polar region of Vesta, and the likely excavation depth is great enough to accom-

modate the largest fragments (43), making it plausible that the south pole basin is the remnant impact scar from the formation of the Vesta family and the site of origin for the HED meteorites.

REFERENCES AND NOTES

- Vesta is the third largest asteroid with a mean diameter of 530 km (P. C. Thomas *et al.*, *Icarus*, in press). All other known basaltic asteroids are <10 km in diameter.
- At its closest distance in May 1996, Vesta was 1.17 AU from Earth, within 0.03 AU of its closest possible approach. At that time, its apparent diameter was 0.62 arc sec, or about 15 pixels across as viewed with WFPC2.
- R. P. Binzel and S. Xu, *Science* **260**, 186 (1993).
- B. H. Zellner *et al.*, *Icarus*, in press.
- The 1996 data were obtained through filters F439W (wavelength of 0.439 μm), F673N (0.673 μm), F791N (0.791 μm), F953N (0.953 μm), and F1042M (1.042 μm) at solar phase angles of about 5° .
- Our limb-finding program models the position of an illuminated margin; this software was calibrated to 0.05 pixel with WFPC2 images of Ganymede and Europa taken in June and July 1995. For purposes of fitting an overall ellipsoidal shape model, the low phase angles of the Vesta observations allow correction of terminator positions to nominal limb positions: maximum nominal correction is 5 km for the 1994 data (0.1 pixel) and 1 km for the 1996 data (0.03 pixel).
- J. Schubart and D. L. Matson, in *Asteroids*, T. Gehrels, Ed. (Univ. of Arizona Press, Tucson, 1979), pp. 84–97.
- E. M. Standish and R. W. Hellings, *Icarus* **80**, 326 (1989).
- N. Wu, in *The Reconstruction of HST Images and Spectra II*, R. J. Hanish and R. L. White, Eds. (Space Telescope Science Institute, Baltimore, MD, 1994), pp. 58–63.
- D. P. Simonelli, *Icarus* **103**, 49 (1993).
- P. C. Thomas, *ibid.* **105**, 326 (1993).
- P. Vanisek and E. J. Krakowsky, *Geodesy: The Concepts* (Elsevier, New York, 1986).
- The position and diameter of the (10°N , 270°W) feature correspond to a geologic feature interpreted to be present on the basis of rotationally-resolved ground-based spectroscopy performed by M. J. Gaffey [*Icarus* **127**, 130 (1997)].
- Because this large structure has a central peak, we chose the term "crater" instead of "basin," as the latter most properly refers to multiringed features.
- H. J. Melosh, *Impact Cratering: a Geologic Process* (Oxford Univ. Press, New York, 1989).
- R. J. Pike, in *Impact and Explosion Cratering*, D. J. Roddy, R. O. Pepin, R. B. Merrill, Eds. (Pergamon, New York, 1977), pp. 489–505.
- W. Hale and R. A. Grieve, *J. Geophys. Res.* **87**, 65 (1982); C. A. Wood and J. W. Head, *Proc. Lunar Planet. Sci. Conf.* **7**, 3629 (1976); C. A. Wood, *ibid.* **11**, 2191 (1980).
- R. J. Pike, *Meteoritics* **20**, 49 (1985).
- P. C. Thomas *et al.*, *J. Geophys. Res.* **86**, 8675 (1981); C. R. Chapman and W. McKinnon, in *Satellites*, J. A. Burns and M. S. Matthews, Eds. (Univ. of Arizona Press, Tucson, 1986), pp. 492–580.
- S. Croft, *Icarus* **99**, 402 (1992).
- R. J. Pike, *Moon* **15**, 463 (1976).
- R. P. Binzel *et al.*, *Icarus*, in press.
- Because of the difficulty of uniquely solving for the photometric function out to the limb, as more fully described in (22), we were limited in our geologic investigation to a northern latitude of 56° and a southern latitude of -44° . Thus, we were unable to measure color ratios of the deepest part of the south pole basin or of the central peak.
- E. Asphaug *et al.*, *Icarus* **120**, 158 (1996).
- D. E. Gault and J. A. Wedekind, *2nd International Colloquium on Mars*, Pasadena, CA, 15 to 18 January 1979, NASA Conference Publication 2072 (NASA, Washington, DC, 1979), p. 29.

Fig. 3. Color ratios as measured along topographic contours around excavated regions interpreted as impact craters on Vesta. Vesta's visible spectrum is dominated by a mafic absorption band near 1 μm , where the ordinate and the abscissa provide measures of the band depth (increasing downward) and band width (increasing to the right), respectively (22). Only the south pole crater shows any color-ratio variation that is correlated with topographic depth, where a clear progression of absorption-band strength is seen over the range +4 to -8 km. (Numerical labels give the average depth in kilometers measured from Vesta's global mean surface level for each contour interval sampled.) The topographic high ridge at latitude 30°S , which we interpret as the rim to the south pole crater, shows a reverse compositional trend from +6 to +10 km (measured at the topographic high point near longitude 330°W), consistent with a composition of excavated material that has been overturned. Dashed lines show variational trends between mixing of pyroxene and olivine ($Px-Ol$: olivine increasing to the right) and the calcium content of the pyroxene (Px : higher-calcium pyroxene increasing downward) based on the convolution of laboratory meteorite spectra (44) through HST filter bandpasses. The data for the potential crater at (10°N , 270°W) are vertically offset by +0.10 for clarity, where their locus falls between the points labeled +4 and +1.



26. S. Chandrasekhar, *Ellipsoidal Figures of Equilibrium* (Yale Univ. Press, New Haven, CT, 1969).
27. D. E. Smith, M. T. Zuber, G. A. Neumann, F. G. Lemoine, *J. Geophys. Res.* **102**, 1591 (1997).
28. M. T. Zuber, D. E. Smith, F. G. Lemoine, G. A. Neumann, *Science* **266**, 1839 (1994); G. A. Neumann, M. T. Zuber, D. E. Smith, F. G. Lemoine, *J. Geophys. Res.* **101**, 16841 (1996).
29. S. C. Solomon, R. P. Comer, J. W. Head, *J. Geophys. Res.* **87**, 3975 (1982).
30. C. D. Brown and R. E. Grimm, *ibid.* **101**, 26057 (1996).
31. S. J. Mackwell, M. E. Zimmerman, D. L. Kohlstedt, D. S. Scherber, *Proceedings of the 35th U.S. Symposium on Rock Mechanics*, Reno, NV, 5 to 7 June 1995, J. Daemen and R. Schultz, Eds. (Balkema, Rotterdam, Netherlands, 1995), pp. 207–214.
32. J. A. Burns and V. S. Safranov, *Mon. Not. R. Astron. Soc.* **165**, 403 (1973).
33. R. A. F. Grieve, P. B. Robertson, M. R. Dence, *Proc. Lunar Planet. Sci. Conf.* **12A**, 37 (1981); H. J. Melosh, *J. Geophys. Res.* **87**, 371 (1982); S. K. Croft, *ibid.* **90**, 828 (1985).
34. There are a few known other instances where D_i/R is suspected to be close to unity. The lunar South Pole–Aitken basin, presently about 2500 km in diameter, has an estimated D_i/R of 0.7 (20), the putative Borealis Basin on Mars has an estimated D_i/R of 0.87 [D. E. Wilhelms and S. W. Squyres, *Nature* **309**, 138 (1984); G. E. McGill, *J. Geophys. Res.* **94**, 2753 (1989)], and the 10-km diameter depression at Deimos's south pole, which has been suggested to be a simple crater [P. C. Thomas, *Icarus* **77**, 248 (1989)], has an estimated D_i/R of ~ 1.5 . The 15-km depression Wien Regio on asteroid 243 Ida has a D_i/R of 0.95, if the asteroid's mean radius is considered [R. Greenberg *et al.*, *ibid.* **120**, 106 (1996)]. However, Wien Regio is located on one end of this very elongate object, where the effective radius of curvature is ~ 10 km; thus, Wien Regio effectively has a D_i/R of ~ 1.5 . Several 10-km craters on the other, even smaller end of Ida have D_i/R 's of about 1 to 1.2.
35. W. Benz and E. Asphaug, *Icarus* **107**, 98 (1994); *Comput. Phys. Commun.* **87**, 253 (1994).
36. E. Asphaug and H. J. Melosh, *Icarus* **101**, 144 (1993).
37. E. Asphaug, *Meteoritics*, in press.
38. S. G. Love and T. J. Ahrens, *Icarus* **124**, 141 (1996).
39. T. B. McCord, J. B. Adams, T. V. Johnson, *Science* **168**, 1445 (1970); H. P. Larson and U. Fink, *Icarus* **26**, 420 (1975).
40. The arguments for a single parent-body source for the HED's are discussed by M. J. Drake [in (7), pp. 765–782] and by G. W. Wetherill [*Philos. Trans. R. Soc. London Ser. A* **323**, 323 (1987)].
41. J. Wisdom, *Nature* **315**, 731 (1985).
42. V. Zappala *et al.*, *Icarus* **116**, 291 (1995); F. Marzari, A. Cellino, D. R. Davis, P. Farinella, V. Vanzani, *Astron. Astrophys.* **316**, 248 (1996).
43. The largest fragment is estimated to be 10 km across. Whether it has the structure of a single coherent fragment or a gravitationally bound group of fragments is unknown, although a conglomerate composition for Vesta fragments is suggested by coincident exposure age peaks for the categories of HED meteorites, as found by O. Eugster and T. Michel [*Geochim. Cosmochim. Acta* **59**, 177 (1995)].
44. M. J. Gaffey, *J. Geophys. Res.* **81**, 905 (1976).
45. Based on observations made by the NASA/European Space Agency Hubble Space Telescope, obtained at the Space Telescope Science Institute (STScI), which is operated by the Association of Universities for Research in Astronomy Inc., under NASA contract NAS 5-26555. Supported in part by STScI grant GO-6481. Helpful suggestions were made by M. Zuber and H. J. Melosh.

26 June 1997; accepted 6 August 1997

Cdc25 Mitotic Inducer Targeted by Chk1 DNA Damage Checkpoint Kinase

Beth Furnari, Nicholas Rhind, Paul Russell*

Arrest of the cell cycle at the G_2 checkpoint, induced by DNA damage, requires inhibitory phosphorylation of the kinase Cdc2 in both fission yeast and human cells. The kinase Wee1 and the phosphatase Cdc25, which regulate Cdc2 phosphorylation, were evaluated as targets of Chk1, a kinase essential for the checkpoint. Fission yeast *cdc2-3w* Δ *cdc25* cells, which express activated Cdc2 and lack Cdc25, were responsive to Wee1 but insensitive to Chk1 and irradiation. Expression of large amounts of Chk1 produced the same phenotype as did loss of the *cdc25* gene in *cdc2-3w* cells. Cdc25 associated with Chk1 in vivo and was phosphorylated when copurified in Chk1 complexes. These findings identify Cdc25, but not Wee1, as a target of the DNA damage checkpoint.

Eukaryotic cells have cell cycle checkpoints that arrest division in response to DNA damage (1, 2). In the case of damage inflicted during the G_2 phase of the cell cycle (gap of time after DNA synthesis, but before mitosis), arrest occurs before the onset of mitosis. In metazoans, G_2 checkpoints are important for the maintenance of genome integrity, allowing time for the repair of damaged DNA, or, in the case of severe

damage, for activation of programmed cell death. In haploid yeast the G_2 checkpoint is required for viability. Understanding how the checkpoint signal intersects with the central machinery controlling progression from the G_2 to the M phase is a major goal of current cell cycle studies.

In the fission yeast *Schizosaccharomyces pombe*, checkpoint arrest in the G_2 phase requires a large number of proteins, many of which are believed to play a direct role in DNA repair. These proteins include Rad3, a kinase related to the ATM protein that is defective in ataxia telangiectasia patients (3). Damaged DNA is presumed

to activate Chk1, a protein kinase that is essential for the checkpoint arrest (4–6). The ultimate target of the checkpoint signal is believed to be Cdc2, the cyclin-dependent kinase that induces mitosis. In the normal cell cycle of fission yeast and mammalian cells, the timing of mitosis is determined by the inhibitory phosphorylation of Cdc2 (7). In fission yeast this phosphorylation occurs on Tyr¹⁵ and is catalyzed by the kinases Wee1 and Mik1, with Wee1 being the most active. Dephosphorylation of Tyr¹⁵ and consequent induction of mitosis is catalyzed by the phosphatase Cdc25. The induction of mitosis is thought to be facilitated by activation of Cdc25 and inhibition of Wee1 activity during the G_2 -M transition. Initial studies suggested that the DNA damage checkpoint operated independently of tyrosine phosphorylation of Cdc2 (8, 9), but a more recent analysis established that inhibitory phosphorylation of Tyr¹⁵ is essential for the checkpoint (10). These findings suggest several mechanisms for Chk1-mediated regulation of Cdc2, including the Chk1-dependent activation of Wee1 or inhibition of Cdc25 (10, 11). We designed genetic and biochemical experiments to test these possibilities.

Cells of the genotype *wee1-50* Δ *mik1*, which lack Mik1 and express temperature-sensitive Wee1, undergo rapid dephosphorylation of Cdc2 on Tyr¹⁵ and induction of mitosis when shifted to the restrictive temperature (12). Irradiation of these cells before the temperature shift causes delay of dephosphorylation of Cdc2 and of entry into mitosis (10). Thus, irradiation induces a transient cell cycle arrest after inactivation of Tyr¹⁵ kinases, potentially by inhibition of Cdc25 activity. An experiment was performed to determine whether this delay was due to an authentic checkpoint mediated by Chk1 kinase. For this experiment we used *chk1*⁺ and Δ *chk1* alleles in a *wee1-50* Δ *mik1* background. Cells synchronized in early G_2 phase were exposed to gamma irradiation or mock irradiated and then shifted from 25° to 35°C. Irradiation caused a ~ 60 -min delay of mitosis in the *chk1*⁺ cells (Fig. 1). This delay is attributable to a reduction in the rate of dephosphorylation of Cdc2 on Tyr¹⁵ (10). In contrast, gamma irradiation did not delay mitosis in Δ *chk1* cells (Fig. 1). Therefore, Chk1 is required for the irradiation-induced delay of mitosis observed after inactivation of Wee1 and Mik1 kinases.

These findings implicate Cdc25 as a potential target of Chk1 regulation, but they do not indicate whether Wee1 may also be regulated by Chk1. We used a *cdc2-3w* Δ *cdc25* strain to address this question. The

Departments of Molecular Biology and Cell Biology, The Scripps Research Institute, La Jolla, CA 92037, USA.

*To whom correspondence should be addressed. E-mail: prussell@scripps.edu.